Pickup ion distributions from three-dimensional neutral exospheres

R. E. Hartle,[1,2] M. Sarantos,[1,2,3] and E. C. Sittler Jr.[1]

Received 19 May 2011; revised 18 July 2011; accepted 27 July 2011; published 7 October 2011.

[1] Pickup ions formed from ionized neutral exospheres in flowing plasmas have phase space distributions that reflect their source's spatial distributions. Phase space distributions of the ions are derived from the Vlasov equation with a delta function source using three-dimensional neutral exospheres. The **ExB** drift produced by plasma motion picks up the ions while the effects of magnetic field draping, mass loading, wave particle scattering, and Coulomb collisions near a planetary body are ignored. Previously, one-dimensional exospheres were treated, resulting in closed form pickup ion distributions that explicitly depend on the ratio r_g/H, where r_g is the ion gyroradius and H is the neutral scale height at the exobase. In general, the pickup ion distributions, based on three-dimensional neutral exospheres, cannot be written in closed form, but can be computed numerically. They continue to reflect their source's spatial distributions in an implicit way. These ion distributions and their moments are applied to several bodies, including He^+ and Na^+ at the Moon, H_2^+ and CH_4^+ at Titan, and H^+ at Venus. The best places to use these distributions are upstream of the Moon's surface, the ionopause of Titan, and the bow shock of Venus.

Citation: Hartle, R. E., M. Sarantos, and E. C. Sittler Jr. (2011), Pickup ion distributions from three-dimensional neutral exospheres, *J. Geophys. Res.*, *116*, A10101, doi:10.1029/2011JA016859.

1. Introduction

[2] The importance of measuring and analyzing pickup ions in order to trace atmospheric composition has been long recognized. These ions originate from neutral sources such as exospheres of planets, moons and comets, and interstellar neutral gases, and are carried away by the **ExB** drift in the flowing plasma. Early examples showing how pickup ions can be used to determine the spatial distributions of the source gases include *Hartle et al.* [1973] and *Hartle and Wu* [1973] for Mercury and *Hartle and Thomas* [1974] for the Moon. More recently, *Hartle and Killen* [2006] reinforced the idea that lower neutral exosphere densities can be derived from ion mass spectrometers than from neutral mass spectrometers. Although beyond the scope of this work, a number of pickup ion measurements have recently been made with these principles and others in mind [see *Sittler et al.*, 2009].

[3] In a recent paper, referred to as Paper 1, *Hartle and Sittler* [2007] derived an expression for the phase space density of pickup ions that accounts for the spatial distribution of the neutral source gas. To keep matters simple, the neutral source was assumed to vary exponentially in the flow direction with a scale height, H; under this simplification it was demonstrated that the ion velocity distribution is explicitly dependent on configuration space through the fundamental ratio r_g/H, where r_g is the ion gyroradius. When $r_g/H \ll 1$, the interaction is fluid, whereas when $r_g/H \gg 1$ it is kinetic. Paper 1 concentrated on the distribution functions, whereas this paper will concentrate on their integrals, yielding densities, velocities, and fluxes. Furthermore, this work extends the formulation of Paper 1 by making the neutral density a three dimensional exosphere [e.g., *Hartle*, 1971] with an arbitrary flow direction and magnetic field. Both papers assume that the flow direction and magnetic field are spatially uniform and remain constant. The latter assumptions are quite relevant to Earth's Moon and moonlike interactions such as the magnetic-free icy bodies at Jupiter and Saturn. These are good approximations in front of (upstream and where the flowing plasma hits the surface) these bodies, but none are good in the wake regions or other regions where electromagnetic disturbances are prevalent (e.g., lunar charged terminators, Alfvèn wings at moons, etc). They are also good approximations in the upstream regions of bow shocks (e.g., Venus, Earth, and Mercury) or ionopauses where there are no shocks (e.g., Titan).

2. Analysis of Ion Pickup Model

2.1. Solution of Vlasov Equation With Source Term

[4] Some of the equations used here are the same as those of Paper 1; consequently they are kept brief but repeated for completeness, while the new relations are expanded

[1]Heliophysics Science Division, NASA Goddard Space Flight Center, Greenbelt, Maryland, USA.
[2]NASA Lunar Science Institute, Moffett Field, California, USA.
[3]Goddard Earth Science and Technology Center, University of Maryland, Baltimore, Maryland, USA.

Copyright 2011 by the American Geophysical Union.
0148-0227/11/2011JA016859

upon (section 2.2). The velocity distribution function of the pickup ions, f(**x**, **v**), is derived from the Vlasov equation

$$\mathbf{v}\cdot\frac{\partial \mathrm{f}}{\partial \mathbf{x}}+\frac{\mathrm{e}}{\mathrm{m}}(\mathbf{E}+\mathbf{v}\times\mathbf{B})\cdot\frac{\partial \mathrm{f}}{\partial \mathbf{v}}=\mathrm{RN}(\mathbf{x})\delta(\mathbf{v}) \tag{1}$$

with an ion source term, where e and m are the pickup ion charge and mass, respectively, **x** is the position vector, **v** is the velocity vector, **B** is the magnetic field, and

$$\mathbf{E}=-\mathbf{V}_b\times\mathbf{B} \tag{2}$$

is the motional electric field resulting from the background plasma velocity $\mathbf{V}_b$. The ion source on the right hand side of (1) is given in terms of the ion production rate, R, the spatial distribution of the neutral source density, N(**x**), and a delta function, $\delta(\mathbf{v})$, describing the velocity distribution of the newly born source ions. In Paper 1 a simple neutral density profile, $N_0\mathrm{Exp}(x/H)$, was used, where the exobase density N_0 is evaluated at x = 0; H is the atmosphere scale height, and x < 0 is the region upstream of the obstacle. Instead of a barometric distribution used in Paper 1, this paper presents solutions of (1) for a generalized three-dimensional exosphere such as the spherically symmetric case described by *Chamberlain* [1963] or the more asymmetrical one like *Hartle and Thomas* [1974] describing He on the Moon. The pickup ion distribution f(**x**, **v**) satisfying the Vlasov equation of (1) is written in the solar rest frame. We note that if equation (1) were written in the frame of the plasma wind, the electric field would vanish. Ion birth at zero velocity is a reasonable approximation because the background plasma velocities (solar wind or rotating magnetospheres) are much greater than velocities of a typical exosphere of atoms and molecules of the neutral source gases.

[5] The coordinates used are Cartesian, where $\mathbf{x} = x\mathbf{i} + y\mathbf{j} + z\mathbf{k}$ and $\mathbf{v} = v_x\mathbf{i} + v_y\mathbf{j} + v_z\mathbf{k}$ in terms of the unit vector triad (**i**, **j**, **k**). To simplify the analysis, one makes the magnetic field uniform and point in the z or **k** direction, whereas x or **i** is the direction of the pickup ion drift velocity, perpendicular to the magnetic field. The pickup ion moves perpendicular to **B** with a drift velocity $\mathbf{V_d} = \mathbf{ExB}/B^2$ whose magnitude is $V_b\mathrm{Sin}\theta_{bv}$, where θ_{bv} is the angle between $\mathbf{V_b}$ and **B**; consequently, the electric field, **E**, is the y or **j** direction. Equation (1) is now written as

$$\nu\frac{\partial f}{\partial \xi}+\eta\frac{\partial f}{\partial \psi}+\left[\eta\frac{\partial f}{\partial \nu}+(1-\nu)\frac{\partial f}{\partial \eta}\right]=\frac{RN_0r_g}{V_d^3}\delta(\nu)\delta(\eta)n'(\xi,\psi) \tag{3}$$

where the v_z component has been integrated out because it is inconsequential to the analysis (pickup ions only have v_x and v_y components) and the dimensionless coordinates used are

$$\xi = x/r_g, \tag{4a}$$

$$\psi = y/r_g, \tag{4b}$$

$$\nu = v_x/V_d, \tag{4c}$$

$$\eta = v_y/V_d, \tag{4d}$$

where ξ and ψ are the x and y coordinates normalized by the ion gyroradius, $r_g = V_d/(eB/m) = V_b\mathrm{Sin}\theta_{bv}/(eB/m)$, in the background plasma of speed, V_d. In (3) n' is an exospheric density normalized by N_0. The x and y velocity components are normalized by $V_d = V_b \sin\theta_{bv}$. However, a z spatial component remains in n' and f. The stationary neutral source gas is assumed to be cold with respect to the moving background plasma. The ions are produced from the neutral gas by photoionization, charge exchange with the background plasma ions and impact ionization resulting from collisions with the background electrons. This leads to

$$R = R_{PI} + R_{CE} + R_{EI} \tag{5}$$

where the reaction rate, R, is usually made up of three components whose type is indicated by the subscripts PI for photoionization, CE for charge exchange, and EI for electron impact. Equation (3) is solved by the method of characteristics that define cycloidal trajectories in terms of the constants of motion

$$\varepsilon = \nu^2 + \eta^2 - 2\nu \tag{6a}$$

$$\kappa = \nu - \psi \tag{6b}$$

$$\begin{aligned}\xi_n^+ &= \xi + \sqrt{2\nu-\nu^2} - \sin^{-1}(\nu-1) - \frac{\pi}{2} - 2\pi n\\ \xi_n^- &= \xi - \sqrt{2\nu-\nu^2} + \sin^{-1}(\nu-1) - \frac{3\pi}{2} - 2\pi n\end{aligned} \tag{6c}$$

where $\varepsilon - 1$ is proportional to the ion kinetic energy in the frame moving with the background plasma and κ is proportional to the ion momentum. The n-th position constants ξ_n^+ and ξ_n^- correspond to n-th positions on the *x* axis in units of r_g, and superscripts + and − refer to $\eta > 0$ and $\eta < 0$, respectively. To fulfill the requirement that the trajectory satisfies $\nu = \eta = 0$ when the ions are born, the energy constant $\varepsilon = 0$ throughout. Physically, ξ_n^+ is the position of the n-th source producing ions with $\eta > 0$ that pass through the observation point ξ, while ions at ξ with $\eta < 0$ are produced at ξ_n^-. Note that for each incremental increase in the index n, the n-th source is further from ξ by 2π.

2.2. Form of Pickup Ion Distributions

[6] A general solution to the Vlasov equation (3) can be written in the form $f = F(\varepsilon, \kappa, \xi_n^+, \xi_n^-)$, where F is an arbitrary function of the constants of motion and $\xi_n^\pm$ are to be read as $\xi_0^\pm, \xi_1^\pm, \xi_2^\pm, \ldots$. The distribution can take the form $f = \delta(\varepsilon)G(\xi_n^+, \xi_n^-, \kappa)$, where G is another function to be specified and related to the form of the exospheric source. The z spatial coordinate normalized to delta, δ, is also in G, but is not shown because the constants of motion are being emphasized. Since the position constants are associated with the sign of η, the distribution naturally separates into

$$f = A\delta(\varepsilon)\left\{G^+\left(\xi_n^+,\kappa\right)S(\eta) + G^-\left(\xi_n^-,\kappa\right)[1-S(\eta)]\right\} \tag{7}$$

where A is a constant related to the source strength, as shown below, the unit step function $S(\eta)$ is 1 or 0 if $\eta \geq 0$ or $\eta < 0$, respectively, and the superscripts on the new func-

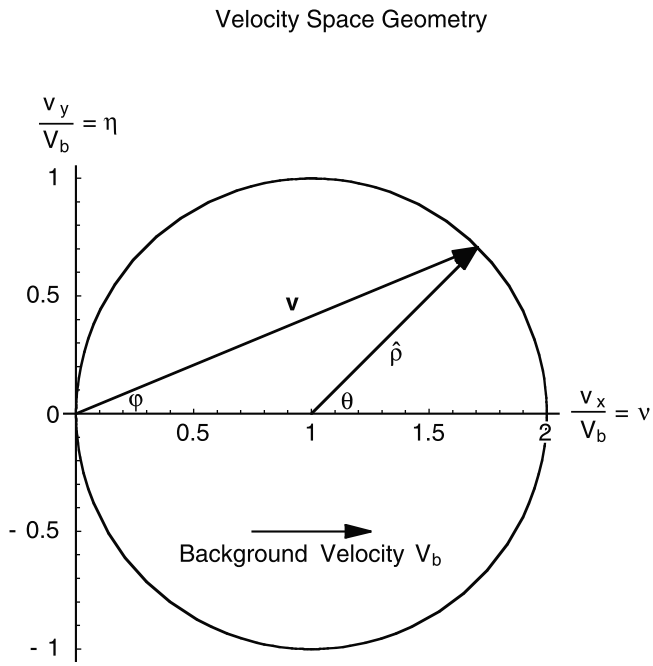

Figure 1. Geometry of pickup ion trajectories in a ring distribution. The abscissa, $\nu = v_x/V_b$, is along the direction of the flowing background plasma, while $\eta = v_y/V_b$ is orthogonal to the flow. The pickup ions move in cycloidal trajectories in the x-y plane. There is no motion along the v_z/V_b direction. The angles θ and φ are defined along with the ion velocity v in the inertial frame and $\hat{\rho}$ in the proper frame of the background flow.

tions G^+ (ξ_n^+, κ) and G^- (ξ_n^-, κ) refer to the sign of η. The property $\delta(2V_d v_x - v_x^2 - v_y^2) = \delta(V_d^2\varepsilon) = (1/V_d^2)\delta(\varepsilon)$ has been applied. The form considered here goes from the one-dimensional source term of Paper 1 to the three-dimensional source term

$$f = A\delta(\varepsilon)\sum_{n=0}^{\infty} \cdot \left\{ \begin{array}{l} G^+\left(\xi + \sqrt{2\nu - \nu^2} - \sin^{-1}(\nu - 1) - \frac{\pi}{2} - 2\pi n, \kappa\right) S(\eta) \\ +G^-\left(\xi - \sqrt{2\nu - \nu^2} + \sin^{-1}(\nu - 1) - \frac{3\pi}{2} - 2\pi n, \kappa\right)[1 - S(\eta)] \end{array} \right\}. \tag{8}$$

[7] There are different ways to parameterize (3) in order to apply the method of characteristics. All involve the description of ν and η as the velocity components of a "ring" distribution (Figure 1). These are constrained by the delta function, $\delta(\varepsilon)$, which defines the velocity circle, $\nu^2 - 2\nu + \eta^2 = 0$, of allowed velocities. This velocity ring of radius unity is centered on ($\nu = 1$, $\eta = 0$). In this paper we consider the change to θ angular coordinates and refer to Paper 1 for other transformations. The x velocity of a pickup ion, ν, and its y velocity, η, (both in units of $V_b \mathrm{Sin}\theta_{bv}$) are related to the polar angle, θ, by $\nu = 1 + \cos\theta$ and $\eta = \sin\theta$, respectively. These parameters are also related by $\nu^2 + \eta^2 = 2(1 + \cos\theta) = 2\nu$ and $\eta = \pm\sqrt{(2(1 + \cos(\vartheta)) - (1 + \cos(\vartheta))^2} = \sin(\vartheta)$. Then, when $-\pi \le \vartheta \le \pi$, it can be shown that

$$\mathrm{f} = A\delta(\varepsilon)\sum_{n=0}^{\infty} \left\{ \begin{array}{l} G^+(\xi + \sin\vartheta + \vartheta - \pi - 2\pi n, \kappa) S(\sin\vartheta) \\ +G^-(\xi + \sin\vartheta + \vartheta - \pi - 2\pi n, \kappa)[1 - S(\sin\vartheta)] \end{array} \right\}. \tag{9}$$

[8] In most cases, $G^+(x, y) = G^-(x, y) \equiv G(x, y)$, and then equation (9) reduces to

$$\mathrm{f} = A\delta(\varepsilon)\sum_{n=0}^{\infty} \{G(\xi + \sin\vartheta + \vartheta - \pi - 2\pi n, \kappa)\} \tag{10}$$

which no longer needs the step function.

[9] As in the simpler example of Paper 1, f is a function of the constants of motion ε and $\xi_n^{\pm}$, and the discontinuous functions $S(\eta)$. Therefore, when the operations in the left hand side of (3) are carried out for $-\pi \le \vartheta \le \pi$, one obtains using equation (8)

$$\mathrm{LHS} = \frac{A}{2}\delta(\eta)\delta(\nu)\sum_{n=0}^{\infty} \cdot \left\{ \begin{array}{l} G^+\left(\xi + \sqrt{2\nu - \nu^2} - \sin^{-1}(\nu - 1) - \frac{\pi}{2} - 2\pi n, \kappa\right) \\ -G^-\left(\xi - \sqrt{2\nu - \nu^2} + \sin^{-1}(\nu - 1) - \frac{3\pi}{2} - 2\pi n, \kappa\right) \end{array} \right\} \tag{11}$$

which is written explicitly as

$$\mathrm{LHS} = \frac{A}{2}\delta(\nu)\delta(\eta)G^+(\xi, -\psi) + \frac{A}{2}\delta(\nu)\delta(\eta)\sum_{j=1}^{\infty} \cdot \{G^+(\xi - 2\pi j, -\psi) - G^-(\xi - 2\pi j, -\psi)\} \tag{12}$$

and finally reduces to

$$\mathrm{LHS} = \frac{A}{2}\delta(\nu)\delta(\eta)G(\xi, -\psi) \tag{13}$$

where $G^+(\xi, -\psi) = G^-(\xi, -\psi) \equiv G(\xi, -\psi)$ has been invoked again, and

$$A = 2\frac{r_g R N_0}{V_d^3} \tag{14}$$

where N_0 is the value of the exospheric density at the nose of the obstacle, and $G(\xi, -\psi, \delta) \equiv n'(\xi, \psi, \delta)$, and the z component $\delta = z/r_g$ is now shown explicitly. Their density and flux (and velocity) are defined respectively as

$$n(\xi, \psi, \delta) = AV_d^2 \int F(\varepsilon, \kappa, \xi^{\pm}) d\nu d\eta \tag{15a}$$

and

$$n\langle v_x\rangle(\xi, \psi, \delta) = AV_d^3 \int \nu F(\varepsilon, \kappa, \xi^{\pm}) d\nu d\eta \tag{15b}$$

Table 1. Parameters Used for Pickup Ion Constituents on Satellites and Planets[a]

Pickup Ion	He^+	Na^+	H_2^+	CH_4^+	H^+
Satellite/Planet	Moon	Moon	Titan	Titan	Venus
V_b	400 km/s	400 km/s	120 km/s	120 km/s	400 km/s
B	8×10^{-5} gauss	8×10^{-5} gauss	5×10^{-5} gauss	5×10^{-5} gauss	10^{-4} gauss
H	498 km	435 km	1116 km	139 km	278 km
M_p	7.35×10^{25} g	7.35×10^{25} g	1.35×10^{26} g	1.35×10^{26} g	4.87×10^{27} g
R_p	1740 km	1740 km	2575 km	2575 km	6050 km
r_c	1740 km	1740 km	4075 km	4004 km	6310 km
r_g	1800 km	10700 km	501 km	3989 km	742 km
r_c/r_g	0.967	0.163	8	1	8.48
r_g/H	3.61	24.6	0.449	28.7	2.67

[a]V_b, background velocity; B, magnetic field; $H = kT_c/mg$, scale height at exobase; M_p, planet/satellite mass; R_p, planet/satellite radius; r_c, exobase radius; r_g, gyroradius. H for $Na^+ = r_c/4$ (see text).

where the ways to perform the integrals of equations (15a, 15b) are shown in Paper 1 as equations (16a, b).

[10] Unlike our formulation in Paper 1, when N is a general function, the ion distribution function f consists of infinite sums and has no closed form. The convergence rate of the series is dependent on exospheric properties and is tested numerically. When r_g is much larger than a neutral gradient scale ("scale height"), the sum at a given velocity vector converges using fewer cycloids than cases when the ion gyroradius is comparable to or less than a neutral scale height. Although equations (8) and (9) are more general, equation (10) can also be used because one cannot think of any reason for which the assumption $G^+(\xi, -\psi, \delta) = G^-(\xi, -\psi, \delta) \equiv G(\xi, -\psi, \delta)$ limits one's ability to describe ejecta from any three-dimensional exosphere.

3. Pickup Ions at Various Bodies

[11] Descriptions of the phase space distributions are adequately covered in Paper 1, even though it refers to one dimensional configuration spaces. This paper will concentrate on the densities and fluxes surrounding three bodies, namely: the Moon, Titan, and Venus. Our formulation is best suited to describing the Moon-solar wind interaction because the lunar atmosphere is a surface-bounded exosphere and the solar wind's magnetic field interacts directly with the lunar surface with essentially no deflection throughout its interaction. Titan is the next least complicated interaction because the atmosphere and ionosphere of this unmagnetized body interact directly with the moving plasma that is Saturn's rotating magnetosphere. On rare occasions Titan will leave the Kronian magnetosphere and be exposed to the solar wind plasma. Exposure only to the magnetospheric plasma will be studied in this paper, where Saturn's magnetic field drapes around Titan as it interacts with this moon. At Titan's position in the magnetosphere the plasma is subsonic and no shock wave is present. The final body studied here, Venus, is also unmagnetized and its atmosphere/ionosphere interacts directly with the supersonic solar wind, thus producing both an ionopause and bow shock.

[12] The primary objective here is to show how the densities, fluxes, and velocities of equations (15a) and (15b) vary on various planes. For example, the ion distribution surrounding all bodies and its moments may be shown in regions at or above the surface of the Moon, the ionopause of Titan, and the shock of Venus, where our formulation gives an *exact solution* of (1). This formulation describes ions in the entire region in front of the Moon because there is essentially no draping of the upstream magnetic field and mass loading down to the surface. The upstream fields of Titan and Venus do experience some draping and mass loading, hence for these latter bodies one must consider planes that are above the ionopause or bow shock, respectively, to minimize the effects of draping and mass loading. Some of the values used in the computations are given in Table 1, including the known light and heavy constituents, He^+ and Na^+ at the Moon, H_2^+ and CH_4^+ at Titan, but only the light constituent H^+ at Venus. One can see that when the bodies have light and heavy constituents, their ratios of r_c/r_g and r_c/H vary as $1/z$ and z^2, respectively, assuming thermal neutral distributions. These are used below to compare some of the results at different bodies.

3.1. Pickup Ions at the Moon

[13] The transport of lunar pickup ions is first plotted in a plane that is applicable to all three bodies; it is in front of the satellite/planet and precedes the flowing plasma that strikes the surface (Moon), ionopause (Titan), or bow shock (Venus). This plane is perpendicular to the planes of the trajectories, it is parallel to the magnetic field, and it is perpendicular to the component of the solar wind velocity, $V_b \sin\theta_{bv}$, where θ_{bv} is the angle between $\mathbf{V_b}$ and $\mathbf{B}$. The solar wind strikes the Moon's dayside surface, creating a void to the flow on the night. This interaction produces an umbra and penumbra in the wake region beyond the terminator, making small perturbations to the solar wind velocity and density and the IMF (for review, *Halekas et al.* [2011]). Pickup ions in these regions should take account of these changes. However, as a first approximation and because such changes are small, other planes, touching down on the surface and normal to the ones just mentioned are also considered. This is in keeping with one of the main goals of this paper to show how the densities, fluxes, and velocities of equations (15a) and (15b) vary on various planes.

[14] In the case of the Moon, one considers He and Na exospheres primarily because these neutral constituents have been detected and studied before. Furthermore, Na^+ and He^+ have been detected by the ion mass spectrometer onboard the Japanese lunar orbiter SELENE/Kaguya [*Yokota et al.*, 2009; *Tanaka et al.* [2009]], and represent excellent test cases to study the effects of neutral mass and scale heights on pickup ion densities and velocities. The He exosphere

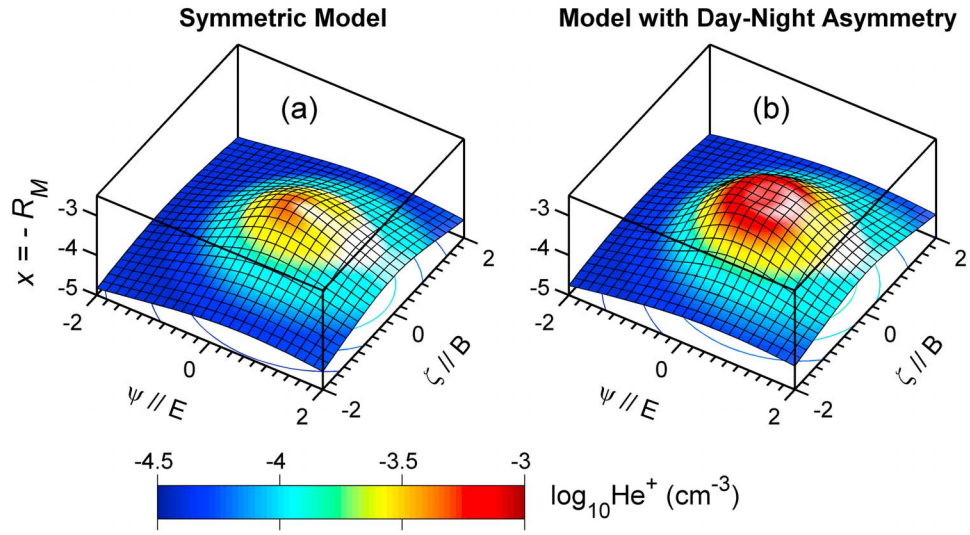

Figure 2. (a, b) Projections of Moon's He^+ density distributions (in Log_{10}) on the plane $\xi = -x_M/r_g = -R_M/r_g$ (R_M is Moon radius), where $\psi = y/r_g$ (parallel to E), and $\zeta = z/r_g$ (parallel to B). A color bar for the densities is on the bottom. Contours of the densities are shown on the plane below the density plot. Figure 2a is the Chamberlain model, which is symmetric, having constant densities and temperatures around Moon. Figure 2b is the Hartle and Thomas model, which is asymmetric, having density and temperature variations around Moon.

and its pickup ion He^+ are studied first followed by Na and its ion Na^+. For simplicity, $\theta_{bv} = 90°$ is considered first (the average field at $\theta_{bv} = 45°$ is then considered in section 3.1.3).

3.1.1. Lunar He^+

3.1.1.1. The Source

[15] Exospheric helium at an inferred density of 2–4 × 10^4 cm^{-3} was detected in the lunar nightside by the Lunar Atmosphere Composition Experiment (LACE) spectrometer that was deployed on the lunar surface by the Apollo 17 spacecraft. The measurements showed a nightside abundance increasing in local time between the terminator and the anti-solar point, which can be reproduced by exospheric models if He atoms are thermally desorbed and almost elastically rebound upon contact with the surface (*Hodges* [1973]; *Hartle and Thomas* [1974]).

[16] Two neutral models were used to describe the distribution of lunar He: the neutral exosphere by *Chamberlain* [1963], a model that is spherically symmetric and has no day-night asymmetry, and the more realistic neutral exosphere of *Hartle and Thomas* [1974], a model that accounts for the day to night temperature and density contrasts and the zero net flux condition of *Hodges* [1973]. In both instances, only the ballistic and escape orbits are considered. They are the major contributors to the density of the neutral gas while the satellite orbits for these bodies are less significant and not well known.

3.1.1.2. The Ions

[17] The first plane considered here is parallel to the magnetic field, perpendicular to the planes of the trajectories, and touches the lunar surface at the point of closest approach (the subsolar point where $\mathbf{V_d} = \mathbf{V_b} \perp \mathbf{B}$).

$$\text{Plane } x = -R_{MOON}.$$

[18] For $\theta_{bv} = 90°$, the planes of the trajectories are parallel to $\mathbf{V_b}$ and the plane of the pickup ion plot touches down on the lunar surface at the sub-solar wind point; i.e., $\xi = -x_M/r_g = -R_M/r_g$. For this model: M = 7.35 × 10^{25} g, T_c = 270 K (a mean lunar surface temperature is chosen for the Chamberlain model), $V_b = 4.0 \times 10^7$ cm^{-1}, and $r_c = 1.73 \times 10^8$ cm, which makes $\lambda(r_c) = 5.05$ so that $\lambda(r) = \lambda(r_c)\,(r_c/r) = 5.05(r_c/r)$. The parameter of equation (14) is A = 6.5 × 10^{-22}, where $R \approx R_{PI} = 10^{-7}$ s^{-1} and $N_0 = 1.3 \times 10^3$ cm^{-3}. Using equation (15a), the lunar pickup ions of Figure 2a (Chamberlain model) form a peak of ~5.6 × 10^{-4} cm^{-3} that is quite observable with the measurement capabilities of modern day ion spectrometers (see *Hartle et al.* [1973]). In fact, all of the densities shown out to ψ and ζ of about two are observable. The peak is shifted along the direction of **E** at $\psi \approx 0.2$ while being centered at $\zeta = 0$. Since the gyroradius is 1.8 × 10^8 cm and the lunar radius is 1.73 × 10^8 cm, the peak is shifted $y = r_g\psi = 3.6 \times 10^7$ cm or ~0.2 lunar radii, respectively. After rounding occurs at the peak, it initially declines almost linearly on a logarithmic scale. Then, when $\psi = -1$ the pickup density range is ~0.25–1 × 10^{-4} cm^{-3} and when $\psi = 1$, the density is ~0.45–2 × 10^{-4} cm^{-3}. When $\psi = -2$, the pickup density range is ~1.8–2.8 × 10^{-5} cm^{-3} and when $\psi = 2$, the density is ~3.5–8.9 × 10^{-5} cm^{-3}.

[19] For comparison with the symmetric model of Chamberlain, the more complex asymmetric lunar He exosphere model of *Hartle and Thomas* [1974], shown in Figure 2b, is used to obtain the realistic He^+ density and flux. This model uses *Hartle* [1971] to account for the day to night temperature and density contrasts. All of the ion model parameters remain the same while the neutral exosphere model reflects the day to night temperature contrast ~385 K/100 K, yielding a density contrast of 1.3 × 10^3/2.2 × 10^4 = 0.059, where $N_0 = 1.3 \times 10^3$ cm^{-3} at the subsolar

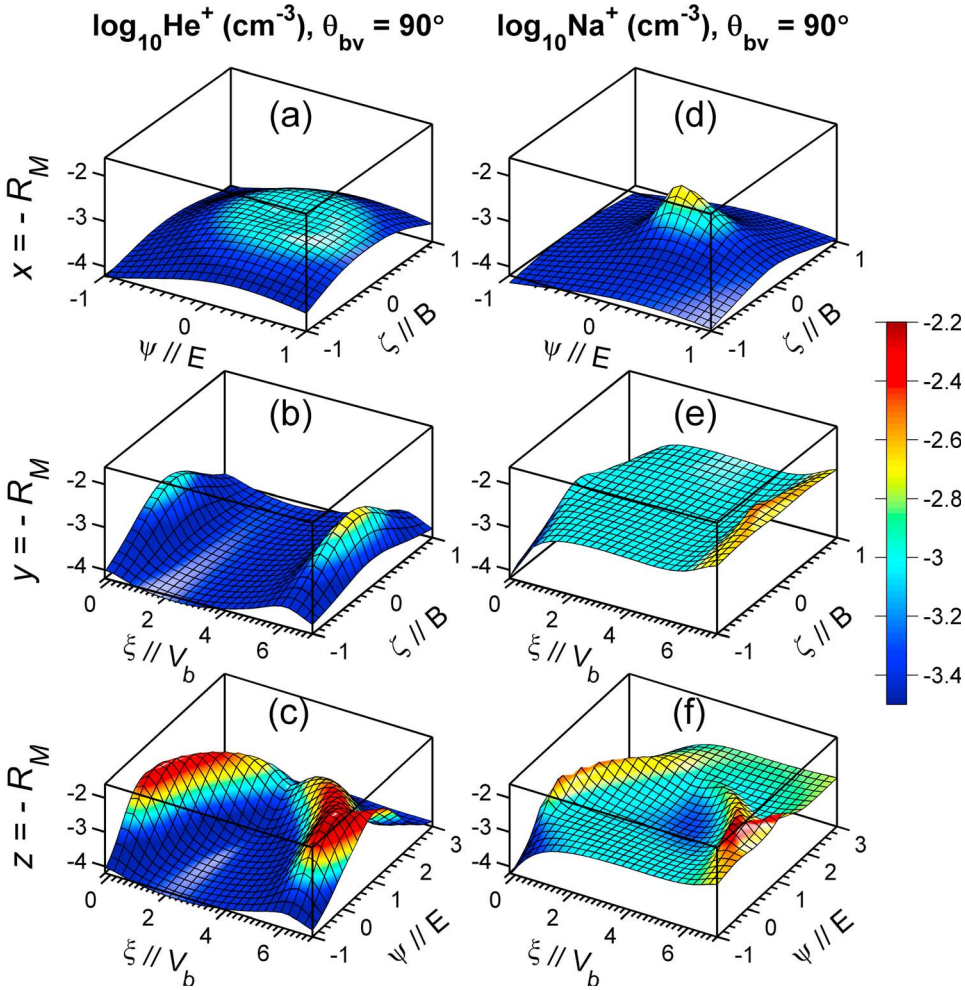

Figure 3. (a–f) Projections of Moon's density distributions (in Log_{10}) on three different planes, where $\theta_{bv} = 90°$ and the left column refers to He^+ while the right to Na^+. A color bar for the densities is on the right. Figures 3a and 3d correspond to the plane $\xi = -x_M/r_g = -R_M/r_g$, with $\psi = y/r_g$ and $\zeta = z/r_g$. Figures 3b and 3e correspond to the plane $\psi = -y_M/r_g = -R_M/r_g$, with $\xi = x/r_g$ and $\zeta = z/r_g$. Figures 3c and 3f correspond to the plane $\zeta = -z_M/r_g = -R_M/r_g$, with $\xi = x/r_g$ and $\psi = y/r_g$.

point. The results of this He^+ pickup ion density distribution are projected on the same plane as the Chamberlain model and are shown in Figures 2b and 3a. Instead of displaying a single peak as in the Chamberlain model, the He^+ ion density near the subsolar point has a dimple surrounded by a rim where the density does peak. This dimple results primarily from the rapid increase in He density and a declining surface temperature as the solar zenith angle increases. A contour plot of the density in this plane, shown in Figure 4a, illustrates the ring-like structure with the two innermost contours having equal densities of ~7.9×10^{-4} cm^{-3}. The density within the rim peaks at ~8.2×10^{-4} cm^{-3}. The rim is centered at $\zeta = 0$ but it is shifted in the **E** direction by ψ ~0.2 (~3.6×10^7 cm or 0.2 lunar radii), which is about the same as Chamberlain's peak shift. However, the ion density variations differ with increasing ψ and ζ.

[20] The differences in the resulting He^+ pickup ion density distributions are clearly a reflection of the different neutral He exospheres. Differences are attributed to the source temperatures, where the actual sub-solar temperature of 385 K was used in the model of *Hartle and Thomas* [1974] while the average temperature of ~273 K was used in the Chamberlain model. The former's higher temperature around the sub-solar point extends the exosphere density to higher altitudes, increasing the number of ions formed, thereby increasing the density downstream. Another reflection of the neutral exosphere source is noted when the projection plane moves outward, say from $\xi = -R_M$ to $-2xR_M$, decreasing the ion density by almost 2 decades or to ~10^{-5} cm^{-3}. The predicted differences by the two models are even more accentuated on the side planes, where the model by *Hartle and Thomas* [1974] predicts a greater enhancement in He^+ levels.

$$\text{Plane } y = -R_{MOON}.$$

[21] To account for the large day/night temperature contrast and the accompanying day/night density change for He, the Hartle and Thomas He exosphere is used for pickup He^+ on the "sides" of the Moon. Figure 3b is a density plot of He^+ in a plane perpendicular to **E** defined by $\psi = -y_M/r_g = -R_M/r_g$

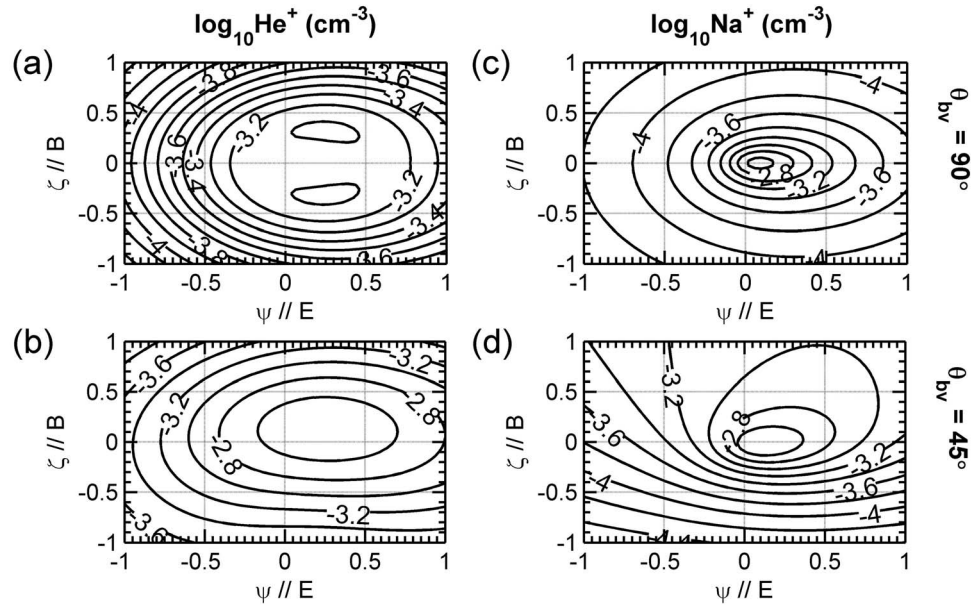

Figure 4. (a–d) Contours of Moon's density distributions (in Log_{10}) on the plane $\xi = -x_M/r_g = -R_M/r_g$, with $\psi = y/r_g$ and $\zeta = z/r_g$, where the left column refers to He^+ and the right to Na^+. Figures 4a and 4c correspond to densities shown in Figures 3a and 3d when $\theta_{bv} = 90°$. Figures 4b and 4d correspond to densities shown in Figures 6a and 6d when $\theta_{bv} = 45°$.

(in units of r_g), where R_M remains the exobase of the Moon, its surface. In this case the variable coordinates are, $\xi = x/r_g$, the flow direction, and $\zeta = z/r_g$, the magnetic field direction. The He^+ gyroradius is larger than a scale height; therefore, the density and flux results will reflect the kinetic approach taken here.

[22] Perhaps the most obvious features of the He^+ density plot in Figure 3b are the density peaks, which are separated by about $\xi = 2\pi$ or $x = 2\pi r_g$ in configuration space. Although not shown, the peaks repeat like this as $\xi \to \infty$, approximating equilibrium about the third or fourth peak (cycloid) downstream of the Moon. The continued increase is a result of the nightside buildup of density and it is clearly a kinetic effect. Recall that a cycloid repeats every 2π (or $x = 2\pi r_g$) and that every 2π an ion's velocity will vanish. At this point and within a neutral scale height, the ion velocity is at its smallest value while the density is near its peak. Therefore, on the plot plane, one expects the neutral density peaks at $\xi \sim 0$, which means that the corresponding pickup ions also peak at $\xi \sim 0$ and then the ion peak repeats every 2π as shown in Figure 3b. The width of the He^+ ion peaks reflect where most of them were born, about a He scale height on both sides of its peak at $(\xi, \zeta) \sim (0, 0)$.

$$\text{Plane } z = -R_{MOON}.$$

[23] In Figure 3c, the He^+ density is plotted in the plane $\zeta = -z_M/r_g = -R_M/r_g$, the lunar exobase in units of r_g. The variable coordinates are, $\xi = x/r_g$, the flow direction, $\psi = y/r_g$, the electric field direction. The density is now shown in a plane that is parallel to the orbits whereas it was shown in a plane perpendicular to the orbits in Figure 3b. The image of a cycloidal trajectory is the obvious feature of this view, which continuously repeats every 2π as $\xi \to \infty$. The appearance of a cycloidal trajectory is possible primarily because the He^+ gyroradius exceeds the He scale height, making it a kinetic plasma. As in the previous view, the greatest numbers of ions are created around the neutral density peak at $(\xi, \psi) \sim (0, 0)$. They are about a scale height thick and are carried down stream in a cycloidal formation, repeating the motion every cycle or 2π. Since most of the ions are produced around $(\xi, \psi) \sim (0, 0)$, they immediately move in a trajectory influenced by the electric and magnetic fields, which is a cycloid. Since they are born bunched together, they remain bunched together and move in identical cycloidal trajectories. The cycloidal trajectory velocity formation is shown in Figure 5a where the $\nu = v_x/V_b$ component vanishes at ion birth, v_x builds up to $2V_b$ after traveling πr_g horizontally and returns to its original vanished state $2\pi r_g$ downstream. At the same time, the $\eta = v_y/V_b$ component is shown in Figure 5b. The velocity v_y also begins by vanishing at ion birth, attains a maximum V_b after traveling $0.5\pi r_g$, goes to zero at πr_g, becomes negative, reaching a peak of $-V_b$ at $1.5\pi r_g$ and then vanishes at $2\pi r_g$. So most of the particles start out in the vicinity of $(\xi, \psi) \sim (0, 0)$ and move upward to about $(\xi, \psi) \sim (\pi, 2)$ and then downward to $(\xi, \psi) \sim (2\pi, 0)$, where they repeat the cycle.

3.1.2. Lunar Na^+

3.1.2.1. The Source

[24] The Na exosphere has been widely studied since its discovery in 1987 [*Potter and Morgan*, 1988] because the sodium spectroscopic properties enable its detection and constant monitoring from Earth. An extensive set of observations, summarized by *Stern* [1999] and *Sarantos et al.* [2010] and continuing to this date, have established that neutral sodium is distributed non-uniformly around the Moon, peaking at the subsolar point with density ~70 atoms cm^{-3}, and extending to altitudes of at least 20 lunar radii. Exospheric models suggest that sodium is liberated from the

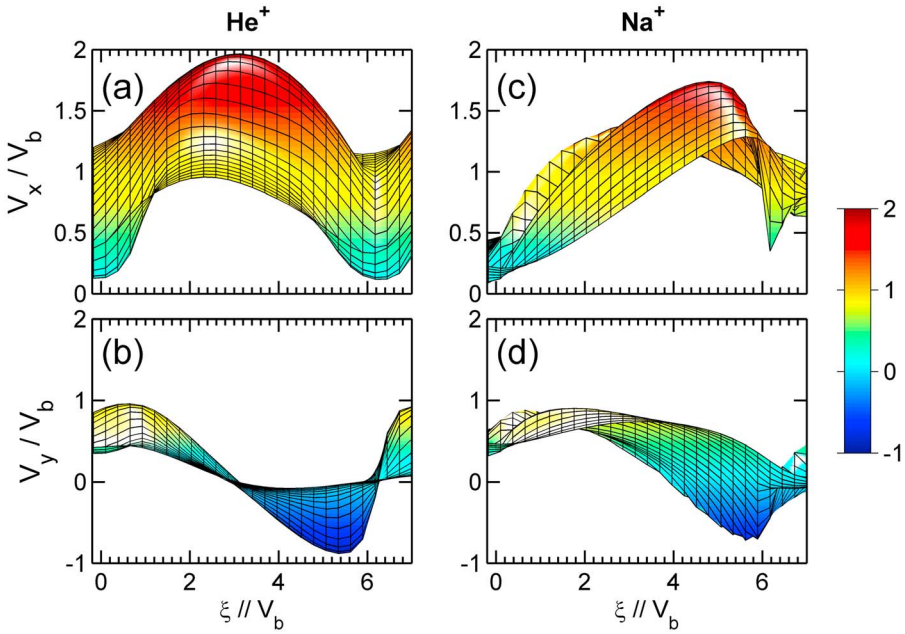

Figure 5. (a–d) Orthogonal projections of Moon's velocity distributions as a function of $\xi = x/r_g$ in the plane $\zeta = -z_M/r_g = -R_M/r_g$. The velocities are $\nu = v_x/V_b$ and $\eta = v_y/V_b$ and are normalized by the background velocity V_b. Visible values of velocities for various $\psi = y/r_g$ are shown at $\theta_{bv} = 90°$. The left column refers to He^+ while the right refers to Na^+. A color bar for the velocities is on the right.

surface primarily by UV photons, with secondary contributions by micrometeoroid impacts and solar wind sputtering (e.g, *Sarantos et al.*, 2010). The resulting exosphere is non-thermal, T~1200 K or more, although a thermal component may exist near the surface owing to the partial thermal accommodation of returning gas material. Because the energy exchange with the surface is not precisely understood, we chose a fit to wide-angle coronagraphic observations which show that: (1) the density decreases as a cosine or cosine-squared function of the solar zenith angle, and (2) that the scale height is variable, with density decreasing with altitude r as r^{-4} at the subsolar point (bound) and as r^{-2} at the poles (escaping) [e.g., *Mendillo et al.*, 1993, 1999; *Potter and Morgan*, 1998].

3.1.2.2. The Ions

[25] As with He^+, the first plane considered for Na^+ has $\theta_{bv} = 90°$, making it parallel to the magnetic field and perpendicular to both the background velocity and the pickup ion trajectories. This plane touches the lunar surface at the point of closest approach, the sub-solar point. All parameters related to the solar wind and Interplanetary Magnetic Field (IMF) are kept the same for direct comparison with He^+ of *Hartle and Thomas* [1974]. The neutral Na used in the model has the distribution $0.5(1 + \cos\vartheta_{sz})\,(r/R_M)^{-(2+2\cos\vartheta_{sz})}$, where θ_{sz} is the solar zenith angle and the factor 0.5 ensures a normalized density. The parameter of equation (14) is $A = 1.47 \times 10^{-17}$, where $R \approx R_{PI} = 5.6 \times 10^{-6}\ s^{-1}$ and $N_0 = 70\ cm^{-3}$. Our results, shown in Figure 3d, indicate that Na^+ forms a peak of ~$2.9 \times 10^{-3}\ cm^{-3}$ that is about a factor of 3.5 more than He^+ from *Hartle and Thomas* [1974] and thus quite observable. The peak occurs at $\zeta = 0$ and $\psi = y/r_g$ ~0.1 or 0.6 lunar radii. The He^+ and Na^+ density distributions are skewed, with their long side being in the direction of the ψ axis or the electric field, **E**. As with He^+, the Na^+ peak is centered at $\zeta = 0$ and after some rounding at the peak, it also declines linearly on a logarithmic scale, but, when plotted on the same spatial scale, the Na^+ density declines slowly with altitude because the Na scale height is large ($H \approx n/(dn/dr)_c = r_c/4$ when $\theta_{sz} = 0$). The skewness is brought out by the differing declines; i.e., the density changes from ~$10^{-3}\ cm^{-3}$ to ~$3.2 \times 10^{-3}\ cm^{-3}$ as ψ changes from 0.0–0.15 while as ψ changes from 0.35–0.2 the density only changes from ~$1.6 \times 10^{-3}\ cm^{-3}$ to ~$2.5 \times 10^{-3}\ cm^{-3}$.

[26] Shown in Figure 3e is the density plane of Na^+ defined by $\psi = -y_M/r_g = -R_M/r_g$. The variable coordinates are $\xi = x/r_g$ and $\zeta = z/r_g$. Peaks are formed again, repeating every $\xi = 2\pi$ or $x = 2\pi r_g$ in configuration space. The peaks appear narrower for Na^+ than for He^+ because the gyroradius for Na^+ is about 5.9 times larger than the gyroradius for He^+, and hence, the spatial scale in the right column of Figure 3 is much wider than that of the left column. Furthermore, the width also reflects where most of the Na^+ ions were born, a distance about a Na scale height from both sides of the peak. Note that the distribution of Na^+ is rather constant between peaks, a result of the large hot Na scale height.

[27] The next plane for Na^+ is shown in Figure 3f and is 90° from the previous one at $\zeta = -z_M/r_g = -R_M/r_g$, where the variable coordinates are $\xi = x/r_g$ and $\psi = y/r_g$. This figure contains the Na^+ cycloidal orbits, which show up thinner than their orbiting counterparts, He^+, due to the larger gyroradius of Na^+. As with He^+, the cycloids for Na^+ are created around the neutral density peak of Na at $(\xi, \psi) \sim (0, 0)$, are about a scale height thick and repeat their cycle every $2\pi r_g$. The Na^+ cycloidal trajectory velocities, ν and η, shown in the same plane in Figures 5c and 5d, respectively. These velocities are moments of the Na^+ distributions and not expected to always follow individual trajectories; e.g., they

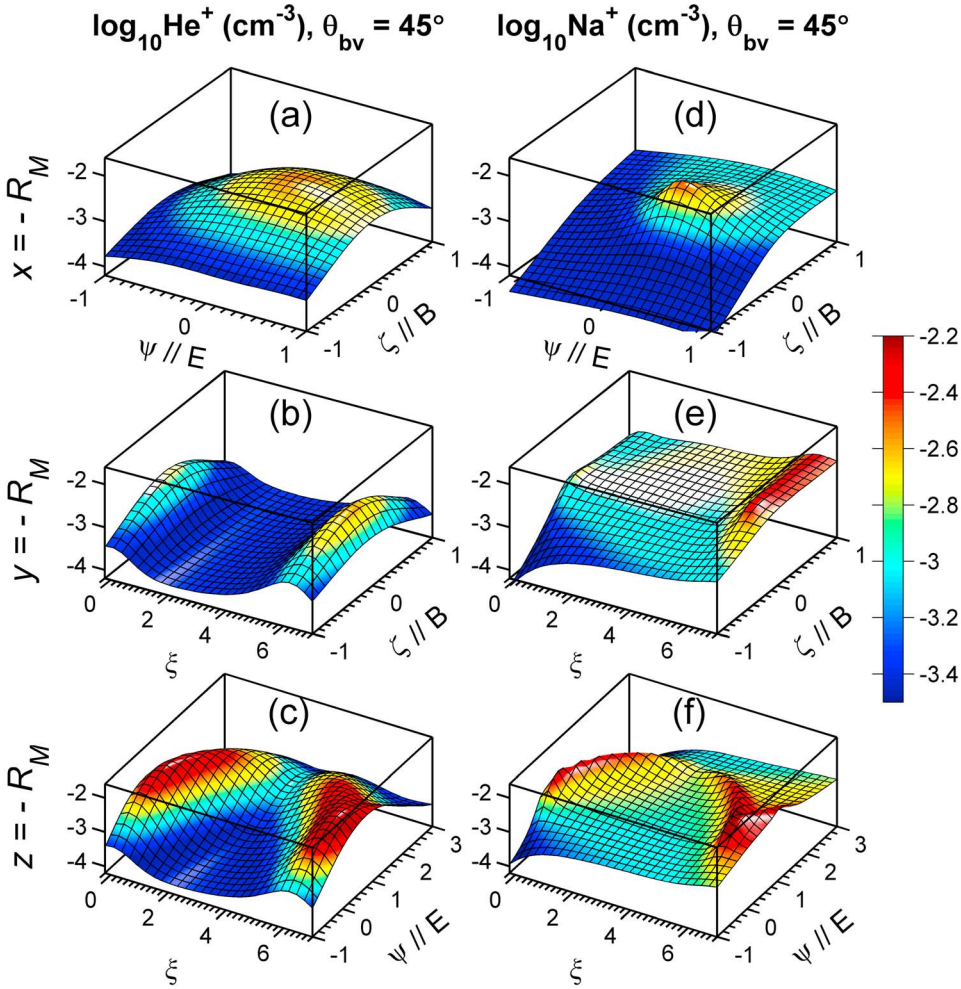

Figure 6. (a–f) Projections of Moon's density distributions (in Log_{10}) on three different planes, where $\theta_{bv} = 45°$ and the left column refers to He^+ while the right refers to Na^+. A color bar for the densities is on the right. Figures 6a and 6d correspond to the plane $\xi = -x_M/r_g = -R_M/r_g$, with $\psi = y/r_g$ and $\zeta = z/r_g$. Figures 6b and 6e correspond to the plane $\psi = -y_M/r_g = -R_M/r_g$, with $\xi = x/r_g$ and $\zeta = z/r_g$. Figures 6c and 6f correspond to the plane $\zeta = -z_M/r_g = -R_M/r_g$, with $\xi = x/r_g$ and $\psi = y/r_g$.

do not reach twice the solar wind velocity. These Na^+ trajectories are quite similar to those for He^+, due in part to the similar density maxima and shapes. Perhaps the biggest difference is their actual size. A Na^+ cycloid span of $2\pi r_g$ is about than 5.8 times (m_{Na}/m_{He}) larger than that of He^+.

[28] Overall, one would naively expect that the kinetic approach is even stronger for sodium since the gyroradius of Na^+ is larger than for He^+. This is not what is observed in these simulations. Instead, Na^+ exhibits a slightly less kinetic nature because it originates from non-thermal neutrals.

3.1.3. Lunar He^+ and Na^+ With B at 45° From Flow Direction

[29] The typical magnetic field direction at one AU is about 45° from the flow direction [*Ness et al.*, 1971]. Recall in equation (1) that the magnetic field **B** is in the $\hat{\mathbf{z}}$ direction and the induced electric field $\mathbf{E} = -\mathbf{V_b} \times \mathbf{B}$ is in the $\hat{\mathbf{y}}$ direction, making the drift velocity $\mathbf{V_d} = \mathbf{E} \times \mathbf{B}/\mathbf{B}^2$ in the $\hat{\mathbf{x}}$ direction with a magnitude $V_b \mathrm{Sin}\theta_{bv} B$. This also says that the plasma flow $\mathbf{V_b}$ is not in the $\hat{\mathbf{x}}$ direction except when $\theta_{bv} = 90°$. Two things change when the plasma flow is not perpendicular to the magnetic field: (1) the ion velocity and gyroradius decrease, and (2) the direction of the pickup ion motion differs from that of the solar wind (they always move perpendicular to the magnetic field). Since our formulation is developed in the pickup ion frame, the planes shown in this section are slices that are rotated by 45° in an inertial Selenocentric frame from their counterparts shown in the previous section. For example, the $x = -R_M$ plane is now tangent to a point that lies 45° from the subsolar point since x is no longer the direction of the Sun-Moon line. Furthermore, the spatial scale, which is normalized to an ion gyroradius, is ~30% smaller in these figures.

[30] He^+ and Na^+ densities at 45° are shown in Figures 6a and 6d, respectively, in a plane defined by $\xi = -x_M/r_g = -R_M/r_g$, which contains the coordinate $\psi = y/r_g$, parallel to the electric field, **E**, and the coordinate $\zeta = z/r_g$, parallel to the magnetic field, **B**. The pickup ion moves perpendicular to **B** in the (ξ, ψ) plane, where ξ is along a component of the solar wind velocity, V_b $\mathrm{Sin}\theta_{bv}$, with $\theta_{bv} = 45°$. These He^+ and Na^+ densities are to be compared with those when $\theta_{bv} = 90°$. The density of He^+ when $\theta_{bv} = 45°$ in Figure 6a no longer has a dimple and rim as the density in Figure 3a when

θ_{bv} = 90°. When θ_{bv} = 45°, the peak is ~3.5 × 10^{-3} cm^{-3} or about 4.3 times larger than when θ_{bv} = 90°. A He^+ density increase is expected as θ_{bv} decreases because the He exobase density increases away from the subsolar point. This is also the main reason the dimple and rim disappear. In contrast, the density of Na^+ in Figure 6d has a shape and peak density similar to that in Figure 3d. As one goes from Figure 3 to Figure 6, θ_{bv} goes to 45°, and one observes that both pickup ions continue to show peak shifts along the ψ coordinate or electric field direction, **E**. This shift is also vividly displayed in Figure 4. Furthermore, when one makes the same angular change in θ_{bv}, one notes that the neutral sources, He and Na, and the corresponding ions, He^+ and Na^+, are symmetric in ζ when θ_{bv} = 90° and are asymmetric in ζ when θ_{bv} < 90°. This is clearly shown by the contours in Figure 4. The peak differences and similarities occurring when θ_{bv} = 45° and 90° are nonlinear, as discussed below.

[31] Figures 6b or 6c and 6e or 6f show the familiar cycloid patterns for He^+ and Na^+ densities, respectively. This time θ_{bv} = 45° and $\zeta = -z_M/r_g = -R_M/r_g$ is the fixed coordinate for Figures 6b and 6e, while $\psi = -y_M/r_g = -R_M/r_g$ is the fixed coordinate for Figures 6c and 6f. In other words, in Figures 6b and 6e the observer is perpendicular to the ion trajectories plane, (ξ, ζ), while in Figures 6c and 6f the observer is in the ion trajectories plane, (ξ, ψ). In each case the ion "sees" the component V_b Sinθ_{bv} of the solar wind velocity, which is perpendicular the magnetic field. As θ_{bv} goes from 90–45° the He exobase densities at the tangent point increase and those of Na decrease. Furthermore, the ion drift velocities decrease by 30% with this angular change.

[32] It is difficult to sort out which of two effects, changes in exospheric density or changes in ion residence time, controls the dependence of pickup ion density on IMF orientation. The exobase density effect seems strong in He^+ because the density in the frontal plane clearly increases at 45°. Even on the sides, where the peaks stay about the same, the valleys increase as θ_{bv} goes from 90–45°. The densities are expected to increase when the ion drift velocities decrease (carried away from birth point at a slower velocity). Since the drift speed decreases by 30%, He^+ ion valley densities increase by this effect. On average, as θ_{bv} goes from 90–45°, Na^+ densities also increase, suggesting that the increase in density due to the effect of slowing down is stronger than the decrease indicated by the neutral exosphere decrease.

3.2. Pickup Ions at Titan

[33] Titan orbits Saturn at about 20 Saturn radii, hence remaining in its magnetosphere most of the time while only occasionally entering the solar wind. At 20 radii, the plasma in Saturn's magnetosphere is subsonic and therefore the moon has no bow shock. Titan has no detectable intrinsic magnetic field, but it has an ionopause on the ram side. These results were found during Voyager 1's flyby of Titan on November 12, 1980 [*Bridge et al.*, 1981; *Ness et al.*, 1981; *Gurnett et al.*, 1981; *Hartle et al.*, 1982; *Neubauer et al.*, 1984; *Sittler et al.*, 2005] and confirmed by many Cassini flybys starting with TA October 26, 2004 [see Titan book by *Brown et al.*, 2009, especially Chapter 16; *Sittler et al.*, 2009]. The major atmospheric constituent, N_2, was observed by the UVS of *Broadfoot et al.* [1981] on Voyager 1, and then by the INMS of *Waite et al.* [2005] onboard Cassini, but not observed beyond the ionopause.

3.2.1. The Sources

[34] Prior to Cassini, several modeling studies [*Keller et al.*, 1998; *Yung*, 1987; *Yung et al.*, 1984; *Toublanc et al.*, 1995] predicted the presence of significant quantities of CH_4 and H_2. CH_4 was subsequently measured in situ by the Ion Neutral Mass Spectrometer (INMS) on Cassini by *Waite et al.* [2005], who reported a density of ~3 × 10^6 cm^{-3} on orbit TA at an exobase altitude of 1429 km (or r_c = 4004 km from center) with a temperature of 145 K. A Chamberlain exosphere is chosen for Titan. In this case $\lambda(r_c)$ = 30.48 and A = 8.96 × 10^{-14}, which includes R_{PI} = 6.5 × 10^{-9} s^{-1} and R_{EI} = 6.6 × 10^{-8} s^{-1}. Measurements of H_2 by INMS on TA and several other Titan encounters suggest an average exobase temperature of 151.2 K at an altitude of 1500 km (or r_c = 4075 km), where the density is ~4 × 10^5 cm^{-3} [*Cui et al.*, 2008]. Using these values, one obtains $\lambda(r_c)$ = 3.59, A = 1.56 × 10^{-16} with R_{PI} = 1.11 × 10^{-9} s^{-1}, R_{EI} = 1.0 × 10^{-9} s^{-1}, R_{EI} = 3.3 × 10^{-9} s^{-1} (for hot and cold electrons, respectively), R_{CE} = 1.4 × 10^{-10} s^{-1}, and R_{PD} = 1.4 × 10^{-9} s^{-1} for photo dissociation. For this model: M = 1.37 × 10^{26} g and V_b = 1.2 × 10^7 cm s^{-1}. On the flybys considered here, Titan was in the magnetosphere where the plasma is subsonic, producing no shock wave but having an ionopause at ~2425 km. The pickup ions CH_4^+ and H_2^+ are borne at and above this altitude from the CH_4 and H_2 exospheres as discussed below.

3.2.2. The Ions

[35] The frontal plane used here is similar to one used at the Moon in that it is perpendicular to the trajectories' plane, which is also perpendicular to the co-rotational flow of the magnetosphere and parallel to the magnetic field. The densities of CH_4^+ and H_2^+ pickup ions are shown in Figures 7a and 7b, respectively. To avoid interaction disturbances, they touch down 2000 km above the exobase, an altitude that is ~1000 km above the ionopause [*Sittler et al.*, 2005]. The density peak for CH_4^+ is ~1.7 × 10^{-4} cm^{-3}, more than 100x smaller than the peak for H_2^+ of ~2.1 × 10^{-2} cm^{-3}. Since the ion production reaction rates are similar, this result at 1000 km above the ionopause is not surprising because H_2 falls off much more slowly than CH_4, even though CH_4 is about 10 times greater at the exobase. As with the Moon, the peaks are centered at ζ = 0 and shifted along the direction of **E** at $\psi \approx 0.2$ for CH_4^+ and $\psi \approx 1$ for H_2^+. Since Titan's radius is 2.57 × 10^8 cm, the peaks are shifted by $y = r_g\psi$ ~8 × 10^7 cm and 5 × 10^7 cm or 0.3 and 0.2 Titan radii, for CH_4 and H_2, respectively. As before, the heaver ion with the larger gyroradius is shifted more. After rounding at the peak, the density initially declines almost linearly on a logarithmic scale.

3.2.3. Comparison to Measurements/Other Simulations

[36] Numerous observations of CH_4^+ and H_2^+ have been made, as reviewed by *Sittler et al.* [2009], but those in the region where the profiles are shown have not been reported yet. However, the hybrid model by *Lipatov et al.* [2011] gives a global picture of the interaction, which covers this region as well. Their results agree quite well with the predicted densities above for CH_4^+ and H_2^+.

3.3. Pickup Ions at Venus

[37] Venus has a number of features that are similar to Titan's, especially because neither has an intrinsic magnetic field, but each has a well-developed ionosphere that carries

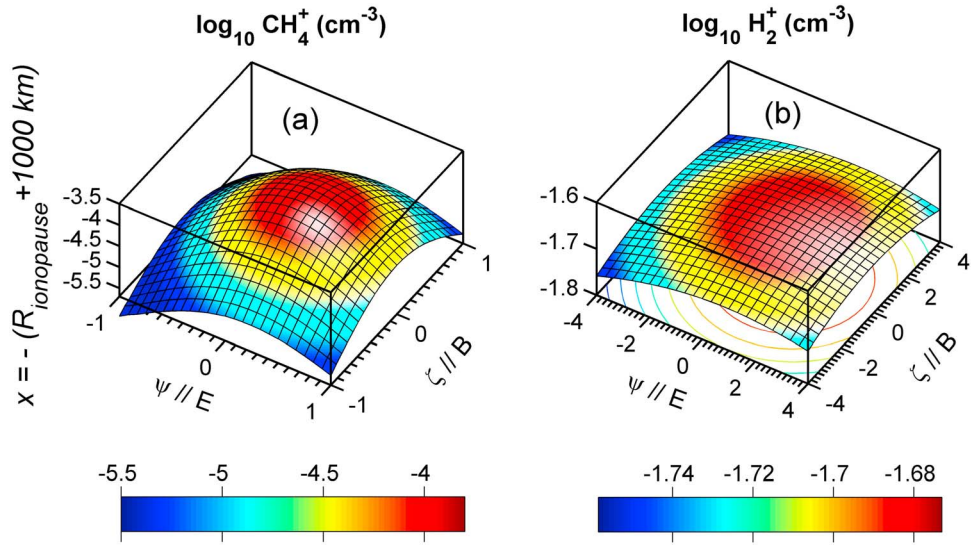

Figure 7. (a, b) Projections of Titan's CH_4^+ and H_2^+ density distributions (in Log_{10}) on the plane $\xi = -(R_I + 1000\ km)/r_g$, where $\psi = y/r_g$ and $\zeta = z/r_g$. This plane is 1000 km above the ionopause radius, R_I and $\theta_{bv} = 90°$. The left column refers to CH_4^+ and the right to H_2^+. Color bars for the densities are on the bottom.

current and forms an ionopause. Venus differs from Titan in that it forms a bow shock ahead of its ionopause, primarily because it is in the supersonic solar wind (see *Russell and Viasberg* [1983] for measurements of interaction).

3.3.1. The Source

[38] Hot H extends beyond the bow shock with densities sufficient enough to produce measurable quantities of pickup H^+. To show this, the following uses *Anderson*'s [1976] analysis of Mariner 5 Lyman α photometer measurements of H Lyman alpha data. He reported an exobase altitude on the dayside of 250 km or r_c = 6305 km from center, using a Venus radius of 6055 km. At the exobase, a cold component (T = 275 K) is present at a density of $2 \times 10^5\ cm^{-3}$ and a hot component (T = 1020 K) is present at a density of $1.3 \times 10^3\ cm^{-3}$. The profile used is also in good agreement with the one suggested by *Cravens et al.* [1980], who developed a theory while using Lyman α measurements from Mariner 5 and 10 together. Choosing a two-component Chamberlain exosphere, one obtains $\lambda(r_c) = 22.68$ and 6.11 for cold and hot H, respectively. The respective cold and hot parameters $A = 1.3 \times 10^{-16}$ and 8.2×10^{-19}, where both use $R_{PI} = 1.6 \times 10^{-7}\ s^{-1}$. The mass of Venus is $M = 4.87 \times 10^{27}$ g and its solar wind background speed $V_b = 4 \times 10^7\ cm\ s^{-1}$.

3.3.2. The Ions

[39] The pickup H^+ density profile from Venus H is shown in Figure 8, which is on a plane parallel to the magnetic field while being perpendicular to the trajectories and the 35° solar wind component [*Luhmann et al.*, 1997]. This plane touches down ~1000 km in front of the bow shock, where the peak density for pickup H^+ is $\sim 6.2 \times 10^{-4}\ cm^{-3}$. As in the previous cases, the peaks are centered at ζ = 0 and shifted along the direction of **E** at ψ ~1 or $y = r_g\psi \sim 7.4 \times 10^7$ cm, corresponding to ~0.12 Venus radii. If the plotting plane touches down ~2000 or 4000 km above the bow shock the peak densities reduce to $\sim 3.5 \times 10^{-4}\ cm^{-3}$ and $\sim 1.9 \times 10^{-4}\ cm^{-3}$, respectively. Similar to the others, the peaks initially fall off linearly on a logarithmic scale.

[40] These pickup ions in the solar wind, just beyond the bow shock of Venus, have not been observed yet. However, there are proton cyclotron wave measurements (PCW) on Venus Express by *Delva et al.* [2009] that may be from ions of exospheric origin. These PCW's from the Venus Express era yield ion densities and corresponding exospheric densities that may be higher than those obtained during the Mariner 5 and 10 eras. Determining the similarities and differences of these measurements is beyond the objective of this text, which is to show how pickup ions may be obtained from a given source.

4. Highlights

[41] The main purpose of the present paper is to extend Paper 1 from a description of the phase space density for pickup ions generated in a one-dimensional exosphere to

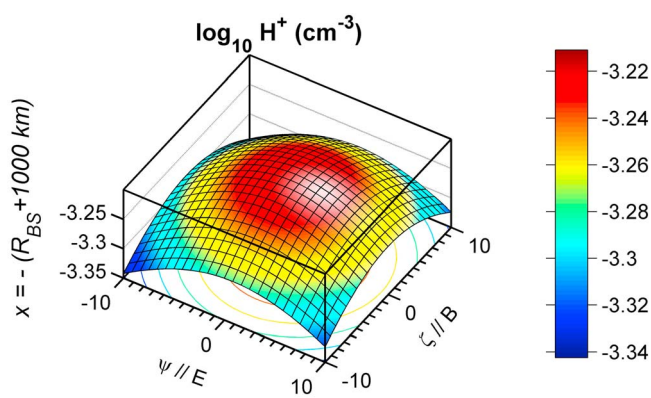

Figure 8. Projection of Venus's H^+ density distribution (in Log_{10}) on the plane $\xi = -(R_{BS} + 1000\ km)/r_g$, where $\psi = y/r_g$ and $\zeta = z/r_g$. This plane is 1000 km above the bow shock radius, R_{BS}, and $\theta_{bv} = 35°$. Contours of the densities are shown on the plane below the density plot. A color bar for the density is to the right.

that of a three-dimensional one that concentrates on its pickup ion moments. As shown in paper 1, the phase space of pickup ions formed from a one-dimensional exosphere is a closed form expression of the spatial distribution of the neutral source gas through its scale height, H, and the ion through its gyroradius, r_g. This is done explicitly through the ratio r_g/H. When the exosphere is extended to three dimensions, the ion distribution still reflects the spatial distribution of the source gas but in this more general case, expressed through equation (8), the spatial relation to the exosphere is no longer explicit and the distribution can no longer be written in closed form. In each case considered, Paper 1 and here, the ambient flow velocity, V_b, and magnetic field, **B**, are uniform.

[42] The ion source considered here is the neutral exosphere that extends outward from its exobase (or surface). New ions are entrained in the flowing plasma that has a magnetic field, **B**, producing an electric field $\mathbf{E} = -\mathbf{V}_b \times \mathbf{B} = BV_b \mathrm{Sin}\,\vartheta_{bv}\hat{\mathbf{y}}$, which picks up the ions and carries them downstream. This formulation is relevant before the background plasma has interacted with the body. At Earth's Moon the flowing plasma, the solar wind, interacts weakly with the dayside of the body; it is absorbed by the surface (except for the highly localized "mini-magnetospheres" that deflect most of the solar wind around them) while its embedded spiral magnetic field is essentially unchanged as it passes through the Moon. Another example is Venus, where the first line of the solar wind's interaction is its bow shock, produced by interactions with its magnetosheath, ionopause, and ionosphere. One is ignoring weaker emanations for this exercise such as particles and wave particle interactions. A final example is Titan, where the flowing plasma is Saturn's rotating magnetosphere. Since its plasma is subsonic, it doesn't have a bow shock, only an ionopause that serves as its first line of interaction with the flowing plasma. Ion pickup of light and heavy ions He^+ and Na^+ are considered at the Moon, H_2^+ and CH_4^+ at Titan, and H^+ at Venus. Some of the parameters used in this study are shown in Table 1.

[43] It was shown how the densities, fluxes, and velocities of equations (15a) and (15b) varied on an upstream plane perpendicular to the planes of the pickup ion trajectories, which is perpendicular to the magnetic field and parallel to the component of solar wind velocity, $V_b\ \mathrm{Sin}\theta_{bv}$. Upstream of the bodies, the formulation is accurate in regions that lie at or above the surface of the Moon, the ionopause of Titan or the shock of Venus. Our studies were more extensive for lunar ions because our formulation for that object is accurate in a wider region of the dayside.

4.1. Moon

[44] Density and flux estimates for two species of lunar origin, He^+ and Na^+, have been produced for the first time. The main results are as follows.

[45] 1. Na^+ is more abundant near the subsolar point but the two species are approximately equally abundant at low altitudes near the terminators.

[46] 2. Densities of ~10^{-2} ions cm^{-3} may be attributed to exospheric origin of these species; measured Na^+ levels could be higher due to an additional surface source of ions [*Elphic et al.*, 1991].

[47] 3. At a given location their relative abundance is a function of the Interplanetary Magnetic Field (IMF) orientation.

[48] 4. Both species exhibit kinetic effects, but the kinetic behavior is more pronounced for He^+ because it originates from thermal neutrals.

[49] The differences may be explained in part by the fact that He increases with solar zenith angle while Na decreases, and in part by the different scale heights. One anticipates these results to aid interpretations of observations from the JAXA orbiter SELENE/Kaguya [*Yokota et al.*, 2009; *Tanaka et al.*, 2009].

[50] In greater detail, He^+ ions from the Moon were considered first when the solar wind was perpendicular to the magnetic field and a Chamberlain model [1963] was compared with one of *Hartle and Thomas* [1974] (Figure 2). The former model is spherically symmetric while the latter accounts for the observed day to night temperature and density contrasts. Both models for He^+ formed peaks of comparable magnitude in pickup ion densities, ~5.6–8.2 × 10^{-4} cm^{-3}, where Chamberlain's was a peak near the subsolar point while Hartle and Thomas was a peak in a rim surrounding the subsolar point. These ions are very observable with today's ion mass spectrometers, and it is not surprising that Kaguya detected them. The peak densities in front of the Moon are shifted off the subsolar point in the direction of the electric field.

[51] A similar analysis was done with lunar Na^+ on the same plane using a source term obtained from neutral Na coronagraphic observations [e.g., *Potter and Morgan*, 1998]. The Na^+ profile shown in Figure 3d forms a peak density of ~2.9 × 10^{-3} cm^{-3}, which is also very observable. This peak is also shifted in the direction of **E**, ~535 km or 0.3 lunar radii, larger than the shift of 0.2 lunar radii for He^+. Also compared with these are the He^+ and Na^+ densities when the angle of the magnetic field to the solar wind velocity was the typical one at $\theta_{bv} = 45°$ (Figures 6a and 6d, respectively). It was found that the He^+ peak at $\theta_{bv} = 45°$ is ~4.3 times larger than the one at $\theta_{bv} = 90°$, while the Na^+ peak is about the same at both positions.

[52] In the foregoing, the densities of the respective light and heavy ions, He^+ and Na^+, were shown on the "front" plane, which is perpendicular to the planes of the trajectories. Densities are also plotted on the "side" planes consisting of planes along the cycloid trajectories, with either a plane parallel to the trajectories planes, $\zeta = z_M/r_g = -R_M/r_g$, or one perpendicular, $\psi = y_M/r_g = -R_M/r_g$. These planes are chosen because $\zeta = -R_M$ avoids running into the wake (e.g., when $\zeta = +R_M$) while $\psi = -R_M/r_g$ avoids ion trajectories that are stopped by the Moon (e.g., when $\psi = +R_M/r_g$). Each of the latter cases is beyond this study. They will require advanced kinetic studies such as treatment of the wake with a Hybrid model (e.g., *Lipatov et al.*, 2011).

[53] Instead, consider the side plane, $\psi = -R_M/r_g$, with the variable coordinates, $\xi = x/r_g$, the flow direction, and $\zeta = z/r_g$, the magnetic field direction. The pickup ion densities for He^+ and Na^+ in this view are shown in Figures 3b and 3e, respectively. Their most obvious feature is the density peaks, produced $(\xi, \psi, \zeta) \sim (0, -R_M/r_g, 0)$, which then reproduce every $\xi = 2\pi$ along with a few additional ions that are added as one passes by the rest of the Moon. These

peaks occur when the average velocity vanishes while on its average cycloid trajectory.

[54] In a plane $\zeta = z_M/r_g = -R_M/r_g$ parallel to the orbits, both He^+ and Na^+ respectively take on the cycloid patterns of individual ions because most of the ions are created around $(\xi, \psi, \zeta) \sim (0, 0, -R_M/r_g)$, where they are born bunched together and remain together as they move downstream (Figures 3c and 3f). After these pickup ions are borne they remain bunched up and repeat their cycle every 2π as $\xi \rightarrow \infty$. The resulting picture is a kinetic view because the He^+ and Na^+ gyroradii exceed their scale heights. Similar to the other view above, since the scale height of He^+ exceeds that of Na^+, the former's density peaks are thicker. When the magnetic field angle to the solar wind velocity is changed from $\theta_{bv} = 90°$ to $\theta_{bv} = 45°$, the He^+ and Na^+ densities are shown in Figures 3c and 6c for He^+ and Figures 3f and 6f for Na^+, respectively. As this angle gets smaller the exobase densities change and the ion drift speed gets smaller. Both of these effects and others contribute to the nonlinear response of the pickup ion distributions. This response results in the average peak to valley increase by He^+ and the average overall increase by Na^+ as $\theta_{bv} = 90°$ goes to $\theta_{bv} = 45°$.

[55] The simulated ion velocities (shown in Figures 5a and 5b for He^+ and Figures 5c and 5d for Na^+) express the kinetic nature of the Moon-solar wind interaction and are consistent with individual cycloid trajectories. For example, the average $\nu = v_x/V_b$ velocity component in Figures 5a and 5c vanishes at ion birth, builds up to a maximum at a horizontal distance π and returns to zero at a distance 2π. Similarly, the $\eta = v_y/V_b$ velocity component in Figures 5b and 5d also vanishes at birth, builds to a maximum at $\pi/2$, vanishes at π, reaches a minimum (negative) at $3\pi/2$ and returns to zero at 2π. In other words, most of the particles start out in the vicinity of $(\xi, \psi, \zeta) \sim (0, 0, -R_M/r_g)$, move upward to about $(\xi, \psi, \zeta) \sim (\pi, 2, -R_M/r_g)$ and then downward to $(\xi, \psi, \zeta) \sim (2\pi, 0, -R_M/r_g)$, where they repeat the cycle. The ion trajectories have a difference in size, wherein the Na^+ cycloid span of $2\pi r_g$ is about than 5.8 times (m_{Na}/m_{He}) larger than that of He^+.

4.2. Titan

[56] We investigated the pickup properties of one light and one heavy ion species, H_2 and CH_4, above Titan's ionopause. The density of CH_4 on TA was $\sim 3 \times 10^6$ cm^{-3} at an exobase of 1429 km and a temperature of 145 K [*Waite et al.*, 2005]. The main ionization of CH_4 comes from electron impact and photoionization. For H2, an average exobase density $N_0 = 4 \times 10^5$ cm^{-3}, at an exobase altitude of 1500 km, with a temperature of 151.2 K have been inferred [*Cui et al.*, 2008]. Ionization of H_2 is from photoionization, electron impact, charge exchange, and photo dissociation. Above their exobases both CH_4 and H_2 neutrals were described using a Chamberlain model.

[57] A front plane ~1000 km above Titan's ionopause [*Sittler et al.*, 2005] is employed to show the densities of the pickup ions CH_4^+ and H_2^+ in Figures 7a and 7b, respectively. This plane is perpendicular to the trajectories' plane and that of co-rotational flow while being parallel to the magnetic field. In this view the peak CH_4^+ density is $\sim 1.7 \times 10^{-4}$ cm^{-3} while that of H_2^+ of $\sim 2 \times 10^{-2}$ cm^{-3}, more than 100 times larger. On a log scale shown, the decrease from these peaks is almost linear. Even though CH_4 is more dense at exobase altitudes, H_2 is much more dense at ionopause heights because it is extended to greater altitudes due to its much larger scale height. The peaks are centered at $\zeta = 0$ and shifted along the direction of **E** at $\psi \approx 0.2$ or 8×10^7 cm for CH_4^+ and $\psi \approx 1$ or 5×10^7 cm for H_2^+, where the heaver ion with the larger gyroradius is shifted the most.

4.3. Venus

[58] This study was limited to exospheric constituents that produce corresponding ions that are dense enough to be measured beyond the bow shock. At present, only hot H measured in Lyman alpha [*Anderson*, 1976] reaches this far. At the exobase of $r_c = 6305$ km, cold H is 2×10^5 cm^{-3} at 275 K and hot H is 1.3×10^3 cm^{-3} at 1020 K. The neutral exosphere is treated by a two-component Chamberlain model from which the ions are mainly produced by photoionization and picked up by the solar wind moving at 400 km s^{-1} with a magnetic field at 35°. In Figure 8 is the resulting picked up H^+ density in plane ~1000 km in front of the bow shock. The peak H^+ pickup density is $\sim 6.2 \times 10^{-4}$ cm^{-3}. Additional density planes of ~2000 km and ~4000 km in front of the bow shock were also considered, with the density decreasing slowly to $\sim 3.5 \times 10^{-4}$ cm^{-3} and $\sim 1.9 \times 10^{-4}$ cm^{-3}, respectively. These peaks are centered at $\zeta = 0$ and shifted along the direction of **E** at $\psi \sim 1$ or 7.4×10^7 cm.

5. Conclusions

[59] Altogether, a pickup ion density peak results when ions are formed upstream of an unmagnetized planet/moon. They are plotted on a plane containing the magnetic field, which is perpendicular to the cycloidal trajectories and the component of the moving plasma, $V_b \mathrm{Sin}\theta_{bv}$. After the peaks are rounded somewhat, they initially fall off linearly for about one or two gyroradii on a log scale. The peaks are symmetric ($\theta_{bv} = 90°$) or asymmetric ($\theta_{bv} < 90°$) about the $\zeta = z//r_g$ axis, which is the magnetic field direction, **B,** and are shifted and skewed along the $\psi = y/r_g$ axis, which is along $\mathbf{E} = -\mathbf{V}_b \times \mathbf{B} = BV_b \mathrm{Sin}\vartheta_{bv}\hat{\mathbf{y}}$. In general, the peak shift, ψ_{peak} in the **E** direction, increases from $-\psi$ as the peak is approached and then the density distribution falls off more slowly beyond the peak, also in the direction of **E**, leading to the distribution's skew. One also uses this method to compute distributions on the sides of those bodies that don't interact with the moving plasma and have surface bound exospheres like the Moon. In those planes where either $\zeta = z_M/r_g = -R_M/r_g$ or, $\psi = y_M/r_g = -R_M/r_g$, the density maximizes where most of the particles are borne and then repeats every $\xi \sim 2\pi$ thereafter. When $\zeta = -R_M/r_g$, one is in the plane of the trajectories where they are more visible when their densities maximize as their velocities vanish around $(\xi, \psi, \zeta) \sim (0, 0, -R_M/r_g)$. Since one is in the plane of the trajectories, these bunched up ions carve out cycloidal trajectories every $\xi \sim 2\pi$. Similarly, when $\psi = -R_M/r_g$, one sees the peak density around $(\xi, \psi, \zeta) \sim (0, -R_M/r_g, 0)$ and then nothing until the next peak appears every $\xi \sim 2\pi$, because one is looking up/down at the trajectory planes.

[60] **Acknowledgments.** Philippa Browning thanks the reviewers for their assistance in evaluating this paper.

References

Anderson, D. E., Jr. (1976), Mariner 5 ultraviolet photometer experiment: Analysis of hydrogen Lyman-alpha data, *J. Geophys. Res.*, *81*, 1213–1216, doi:10.1029/JA081i007p01213.

Bridge, H. S., et al. (1981), Plasma observations near Saturn: Initial results from Voyager 1, *Science*, *212*, 217–224, doi:10.1126/science.212.4491.217.

Broadfoot, A. L., et al. (1981), Extreme ultraviolet observations from Voyager 1 encounter with Saturn, *Science*, *212*, 206–211, doi:10.1126/science.212.4491.206.

Brown, R. H., J.-P. Lebreton, and J. H. Waite (Eds.) (2009), *Titan From Cassini-Huygens*, Springer, Dordrecht, Netherlands.

Chamberlain, J. W. (1963), Planetary corona and atmospheric evaporation, *Planet. Space Sci.*, *11*, 901–960, doi:10.1016/0032-0633(63)90122-3.

Cravens, T. E., T. I. Gombosi, and A. F. Nagy (1980), Hot hydrogen in the exosphere of Venus, *Nature*, *283*, 178–180, doi:10.1038/283178a0.

Cui, I., R. V. Yelle, and K. Volk (2008), Distribution and escape of molecular hydrogen in Titan's thermosphere and exosphere, *J. Geophys. Res.*, *113*, E10004, doi:10.1029/2007JE003032.

Delva, M., M. Volwerk, C. Maselle, J. Y. Chaufray, J. L. Bertaux, and T. L. Zang (2009), Hydrogen in the extended Venus exosphere, *Geophys. Res. Lett.*, *36*, L01203, doi:10.1029/2008GL036164.

Elphic, R. C., H. O. Funsten, B. L. Barraclough, D. J. McComas, M. T. Paffet, D. T. Vaniman, and G. Heiken (1991), Lunar surface composition and solar wind–induced secondary ion mass spectrometry, *Geophys. Res. Lett.*, *18*, 2165–2168, doi:10.1029/91GL02669.

Gurnett, D. A., W. S. Kurth, and F. L. Scarf (1981), Plasma waves near Saturn: Initial results from Voyager 1, *Science*, *212*, 235–239, doi:10.1126/science.212.4491.235.

Halekas, J. S., Y. Sato, G. T. Delory, and W. M. Farrell (2011), New views of the lunar plasma environment, *Planet. Space Sci.*, doi:10.1016/j.pss.2010.08.011, in press.

Hartle, R. E. (1971), Model for rotating and nonuniform planetary exospheres, *Phys. Fluids*, *14*, 2592, doi:10.1063/1.1693379.

Hartle, R. E., and R. Killen (2006), Measuring pickup ions to characterize the surfaces and exospheres of planetary bodies: Applications to the Moon, *Geophys. Res. Lett.*, *33*, L05201, doi:10.1029/2005GL024520.

Hartle, R. E., and E. C. Sittler Jr. (2007), Pickup ion phase space distributions: Effects of atmospheric spatial gradients, *J. Geophys. Res.*, *112*, A07104, doi:10.1029/2006JA012157.

Hartle, R. E., and G. E. Thomas (1974), Neutral and ion exosphere models for lunar hydrogen and helium, *J. Geophys. Res.*, *79*, 1519–1526, doi:10.1029/JA079i010p01519.

Hartle, R. E., and C. S. Wu (1973), Effects of electrostatic instabilities on planetary and interstellar ions in the solar wind, *J. Geophys. Res.*, *78*, 5802–5807, doi:10.1029/JA078i025p05802.

Hartle, R. E., K. W. Ogilvie, and C. S. Wu (1973), Neutral and ion-exospheres in the solar wind with applications to Mercury, *Planet. Space Sci.*, *21*, 2181–2191, doi:10.1016/0032-0633(73)90192-X.

Hartle, R. E., E. C. Sittler Jr., K. W. Ogilvie, J. D. Scudder, A. J. Lazarus, and S. K. Atreya (1982), Titan's ion exosphere observed from Voyager 1, *J. Geophys. Res.*, *87*, 1383–1394, doi:10.1029/JA087iA03p01383.

Hodges, R. R. (1973), Helium and hydrogen in the lunar atmosphere, *J. Geophys. Res.*, *78*, 8055–8064, doi:10.1029/JA078i034p08055.

Keller, C. N., V. G. Anicich, and T. E. Cravens (1998), Model of Titan's ionosphere with detailed hydrocarbon ion chemistry, *Planet. Space Sci.*, *46*, 1157–1174, doi:10.1016/S0032-0633(98)00053-1.

Lipatov, A., E. C. Sittler, R. E. Hartle, J. F. Copper, and D. G. Simpson (2011), Background and pickup ion velocity distribution dynamics in Titan's plasma environment: 3D hybrid simulation and comparison with CAPS observations, *Adv. Space Res.*, *48*, 1114–1125, doi:10.1016/j.asr.2011.05.026.

Luhmann, J. G., S. H. Brecht, J. R. Sprieter, S. S. Stahra, R. S. Steinolfson, and A. F. Nagy (1997), Global models of the solar wind interaction with Venus, in *Venus II*, edited by S. W. Bougher, D. M. Hunten, and R. J. Phillips, pp. 33–59, Univ. of Ariz. Press, Tucson.

Mendillo, M., B. Flynn, and J. Baumgardner (1993), Imaging experiments to detect an extended sodium atmosphere on the Moon, *Adv. Space Res.*, *13*, 313–319, doi:10.1016/0273-1177(93)90085-P.

Mendillo, M., J. Baumgardner, and J. Wilson (1999), Observational test for the solar wind sputtering origin of the Moon's extended sodium atmosphere, *Icarus*, *137*, 13–23, doi:10.1006/icar.1998.6042.

Ness, N. F., A. J. Hundhausen, and S. J. Bame (1971), Observations of the interplanetary medium: Vela 3 and Imp 3, 1965–1967, *J. Geophys. Res.*, *76*, 6643–6660, doi:10.1029/JA076i028p06643.

Ness, N. F., M. H. Acuna, R. P. Lepping, J. E. P. Connerney, K. W. Behannon, L. F. Burlaga, and F. M. Neubauer (1981), Magnetic field studies by Voyager 1: Preliminary results at Saturn, *Science*, *212*, 211–217, doi:10.1126/science.212.4491.211.

Neubauer, F. M., D. A. Gurnett, J. D. Scudder, and R. E. Hartle (1984), Titan's magnetospheric interaction, in *Saturn*, edited by T. Gehrels and M. S. Matthews, pp. 760–787, Univ. of Ariz. Press, Tucson.

Potter, A. E., and T. H. Morgan (1988), Extended sodium exosphere of the Moon, *Geophys. Res. Lett.*, *15*, 1515–1518, doi:10.1029/GL015i013p01515.

Potter, A. E., and T. H. Morgan (1998), Coronagraphic observations of the lunar sodium exosphere near the lunar surface, *J. Geophys. Res.*, *103*, 8581–8586, doi:10.1029/98JE00059.

Russell, C. T., and O. Viasberg (1983), The interaction of the solar wind with Venus, in *Venus*, edited by D. M. Hunten et al., pp. 873–940, Univ. of Ariz. Press, Tucson.

Sarantos, M., R. M. Killen, A. S. Sharma, and J. A. Slavin (2010), Sources of sodium in the lunar exosphere: Modeling using ground-based observations and spacecraft data of the plasma, *Icarus*, *205*, 364–374, doi:10.1016/j.icarus.2009.07.039.

Sittler, E. C., R. E. Hartle, A. F. Vinas, R. E. Johnson, H. T. Smith, and I. Muller-Wodarg (2005), Titan's interaction with Saturn's magnetosphere: Voyager 1 results revisited, *J. Geophys. Res.*, *110*, A09302, doi:10.1029/2004JA010759.

Sittler, E. C., R. E. Hartle, C. Bertucci, A. Coates, T. Cravens, I. Dandouras, and D. Shemansky (2009), Energy deposition processes in Titan's upper atmosphere and its induced magnetosphere, in *Titan From Cassini-Huygens*, chap. 16, edited by R. H. Brown, J.-P. Lebreton, and J. H. Waite, Springer, Dordrecht, Netherlands.

Stern, S. A. (1999), The lunar atmosphere: History, status, current problems, and context, *Rev. Geophys.*, *37*, 453–491, doi:10.1029/1999RG900005.

Tanaka, T., et al. (2009), First in situ observation of the Moon-originating ions in the Earth's magnetosphere by MAP-PACE on SELENE (KAGUYA), *Geophys. Res. Lett.*, *36*, L22106, doi:10.1029/2009GL040682.

Toublanc, D., J. P. Parisot, D. Gautier, F. Raulin, and C. P. McKay (1995), Photochemical modeling of Titan's atmosphere, *Icarus*, *113*, 2–26, doi:10.1006/icar.1995.1002.

Waite, J. H., et al. (2005), Ion neutral mass spectrometer results from the first flyby of Titan, *Science*, *308*, 982–986, doi:10.1126/science.1110652.

Yokota, S., et al. (2009), First direct detection of ions originating from the Moon by MAP-PACE IMA onboard SELENE (KAGUYA), *Geophys. Res. Lett.*, *36*, L11201, doi:10.1029/2009GL038185.

Yung, Y. L. (1987), An update of nitrile photochemistry on Titan, *Icarus*, *72*, 468–472, doi:10.1016/0019-1035(87)90186-2.

Yung, Y. L., M. Allen, and J. P. Pinto (1984), Photochemistry of the atmosphere of Titan: Comparison between model and observations, *Astrophys. J. Suppl.*, *55*, 465, doi:10.1086/190963.

R. E. Hartle, M. Sarantos, and E. C. Sittler Jr., Heliophysics Science Division, NASA Goddard Space Flight Center, Greenbelt, MD 20771, USA. (richard.e.hartle@nasa.gov)